From discrete element method (DEM) to 2D Synthetic Seismic Modelling

Roderick Perez[1]* and Stuart Hardy[2]

Abstract

Fault complexity in seismic data can be more accurately represented by integrating geomechanical simulation and forward seismic modelling. A multi-layer stratigraphic model subjected to progressive deformation was constructed using the Discrete Element Method (DEM). Acoustic impedance fields derived from mechanical evolution provided the basis for calculating vertical reflection coefficients, which were then convolved with zero-phase Ricker wavelets using a 1D approach to produce synthetic seismic sections. Compared to conventional planar-fault representations, the resulting images display intricate reflector terminations, and amplitude dimming associated with distributed fault damage and rotated blocks. These results highlight that even a single fault, when modelled with physics-based deformation, produces richer and more varied seismic responses than matrix-deformation/warping approaches used to create labelled training datasets, providing a more geologically reliable basis for AI fault-segmentation and interpretation.

Introduction

Faults are fundamental geological structures that play a critical role in the generation, migration, and entrapment of hydrocarbons (Kim et al., 2004; Gudmundsson et al., 2010; Zeng and Liu, 2010; Ferrill et al., 2014; Peacock et al., 2017; Gong et al., 2019). Rather than simple breaks or cracks, faults are three-dimensional volumes of distributed deformation with petrophysical properties that differ from the host rock; this internal heterogeneity controls reflectivity and fluid flow and must be honoured when generating credible synthetics (Botter et al., 2014). Despite important advances in acquisition and imaging, interpretation remains challenging due to limited resolution, noise, and stratigraphic-structural ambiguity (Gunderson et al., 2022; Ma et al., 2024). Synthetic seismic modelling helps to bridge geology and data, but many traditional approaches rely on idealised geometry that washes out realistic fault-zone complexity (Alcalde et al., 2017; Zeng and Liu, 2010; Botter et al., 2014; Peacock et al., 2017). Here we integrate Discrete Element Method (DEM)-based mechanical modelling with 1D seismic forward modelling to move beyond idealised planar faults and demonstrate how structurally realistic models generate richer, more interpretable signatures.

In petroleum geoscience, a fault is often defined as a planar discontinuity in a rock volume across which significant displacement has occurred due to tectonic stresses (North, 1985). Interpreting faults from seismic data is a cornerstone of exploration and development workflows (Alcalde et al., 2017; Butler, 2023). The delineation of fault geometry is essential not only for understanding the structural framework but also for predicting compartmentalisation, assessing trap integrity, and optimising well placement (Perez et al., 2024). Interpretation methods rely heavily on the recognition of lateral discontinuities in seismic reflections, such as abrupt amplitude terminations, vertical offsets, or phase changes (Kanasewich and Phadke, 1988; Ercoli et al., 2023). These are often enhanced through seismic attributes and advanced visualisation techniques (Chopra and Marfurt, 2007). However, seismic fault interpretation is not limited to detection; it also includes mapping the geometry, extent, and character of faults and associated damage zones (Planke et al., 2005).

Despite the advances in acquisition and imaging, fault interpretation remains challenging due to limited vertical and horizontal resolution, imaging noise, and ambiguities arising from overlapping structural and stratigraphic features (Romberg, 2002; Chopra and Marfurt, 2007). Some faults are barely visible or even seismically silent, particularly when they occur below tuning thickness or within noisy intervals (Slejko et al., 2011, Reicherter et al., 2023; Ercoli et al., 2023). As a result, interpreters must incorporate geological intuition, attribute-driven analysis, and increasingly, data-driven machine learning techniques to reduce uncertainty and bias (Freeman et al., 2010; Paxton et al., 2022). Nevertheless, these methods are ultimately limited by the accuracy of the subsurface representations used in training or calibration (Khosro et al., 2024).

Synthetic seismic modelling is a powerful tool to bridge geological understanding and seismic imaging (Vizeu et al., 2022). However, many traditional forward modelling approaches rely on simplified geometries and assumptions, such as perfectly planar interfaces, horizontally layered media, or artificial fault shapes generated using geometric routines (Mirkamali et al., 2023). While computationally convenient, these models lack the structural realism

[1] OMV | [2] ICREA - Institució Catalana de Recerca i Estudis Avançats

* Corresponding author, E-mail: roderick.perezaltamar@omv.com, roderickperezaltamar@gmail.com

DOI: xxx

and complexity observed in nature, which can lead to oversimplified and potentially misleading seismic responses (Oakley et al., 2023; Li et al., 2023). In this context, physics-based approaches that simulate fault growth and rock failure from first principles offer an opportunity to generate more representative seismic models rooted in geomechanics (Diao et al., 2024; Boyet et al., 2023).

The DEM, originally developed by Cundall and Strack (1979), provides a mesh-free approach to model large deformations and discontinuities, allowing faults and fractures to emerge as natural responses to applied boundary conditions and mechanical properties. In DEM, rock masses are represented as assemblies of rigid or deformable particles that interact via normal and shear contact forces. This framework has been used to model a wide variety of geological structures, including shear zones, fault-related folds, salt diapirs, and strike-slip fault systems (Morgan and Boettcher, 1999; Egholm et al., 2008; Hardy, 2018; Liu and Konietzky, 2018). Unlike continuum-based approaches, DEM can handle fragmentation, rotation, and sliding explicitly, making it well-suited for a more realistic geological fault evolution simulation.

More recently, DEM has been implemented as a practical modelling tool tailored to geological applications. DEM simulates deformation using rigid circular particles, allowing faults, splays, and complex fracture networks to emerge spontaneously from mechanical interactions (Botter et al., 2014; Cardozo and Hardy, 2023). The DEM method has been applied to problems ranging from caldera collapse to deltaic growth strata and provides an accessible yet robust platform for exploring the mechanical underpinnings of geological structures (Hardy, 2008; 2016; 2018; 2019a, 2019b; Hardy and Finch, 2007; Hardy et al., 2009).

Botter et al. (2014) explicitly present a two-dimensional proof-of-concept: they use 2D DEM to simulate faulting in a sandstone shale sequence and apply 2D seismic imaging to test how illumination direction and frequency affect the resulting image. They also note that the same physics-based workflow can be generalised to 3D for a more realistic representation of fault architecture and wavefield interactions. The study shows that mechanically consistent, non-planar fault models better explain seismic signatures in structurally heterogeneous domains and help bridge conceptual geology and synthetic seismic responses.

By integrating discrete element modelling with seismic forward modelling approaches presented here, we aim to go beyond idealised planar faults and demonstrate how structurally realistic models generate richer and more interpretable seismic signatures. This not only complements modern data-driven techniques but also reinforces the importance of geomechanically consistent models for improving seismic interpretation accuracy in complex faulted terrains.

In this study, we utilise a DEM-based model to simulate the development of a synthetic fault system along a 45-degree fault plane. Each circular element in the model is assigned compressional velocity (V_p) and density (ρ) values, enabling the computation of acoustic impedance once deformation occurs. The resulting impedance distribution is used to calculate vertical reflection coefficients, which are then convolved (1D vertical incidence) with a synthetic and idealised zero-phase Ricker wavelet to produce a pseudo-seismic section that captures the dynamic evolution of faulting and associated displacement.

By explicitly modelling the mechanical response of circular DEM elements that interact through the frictional-cohesive contact law, rather than as a purely pre-bonded continuum, the DEM approach naturally reproduces complex fault-zone features such as irregular fault traces, rotated blocks, and a narrow zone of closely spaced splays elements often missing from traditional geometric models. Unlike earlier work that examined fault-related seismic responses using kinematic or continuum models or attribute-based analysis of existing data without explicitly propagating a mechanically consistent, strain-dependent property field into the synthetics (Townsend et al., 1998; Couples et al., 2007; Dutzer et al., 2010; Long and Imber, 2010; Iacopini and Butler, 2011) our workflow translates the full physical output of DEM simulations into synthetic seismic data. This makes it tractable to produce many geologically consistent examples for interpretation studies and method development, including machine-learning training and benchmarking. In terms of realism, our 1D synthetics reproduce tuning, reflector terminations, and diffraction-like edge responses driven by vertical sampling across lateral terminations, but they do not capture the full diffraction and survey-dependent illumination effects that Pre-Stack Depth Migration (PSDM) imaging handles (Lecomte et al., 2015; Botter et al., 2016). Future work will therefore couple the same mechanical models to PSDM to quantify the additional effects of lateral wave propagation and acquisition geometry.

Methodology

We adopt the DEM formulation described in Cardozo and Hardy (2023). In this 2D lattice- solid variant (Mora and Place, 1993, 1994; Place et al., 2002), a rock volume is discretised into rigid circular elements that interact through normal and tangential contact forces; bonds break irreversibly when a threshold is exceeded, and elements also experience gravity and viscous damping. Motions are advanced with a velocity-Verlet integrator, and a time step linked to element mass (Δt), which ensures numerical stability.

For two bonded elements the normal (radial) force is

$$F_n = \begin{cases} K_n(1-R), & if\ r-R < r_0R \quad (internal\ bond); \\ K_n(1-R) & if\ r < R \quad (compressive\ broken\ bond); \\ 0 & if\ r \geq R \quad (tensional\ broken\ bond). \end{cases} \tag{1}$$

where K_n is the normal spring stiffness, r the instantaneous centre–centre distance, R the equilibrium distance (sum of radii), and r0 the dimensionless bond-breaking strain. A bond fails irreversibly when $r - R < r_0R$; thereafter no tensile attraction exists, although a repulsive force is retained for $r \leq R$.

In the frictional-cohesive formulation all bonds start broken. Normal contact forces still follow Equation 1, but shear resistance is added through a tangential spring whose magnitude is capped by a Coulomb criterion:

$$F_s = \min(K_sX_s + C_0, \mu F_n) \tag{2}$$

with K_s the shear stiffness, X_s the accumulated tangential displacement, C_0 a cohesive term, and μ the inter-element friction coefficient (Cundall and Strack, 1979; Mora and Place, 1994). If contact is lost all forces at that pair are reset to zero.

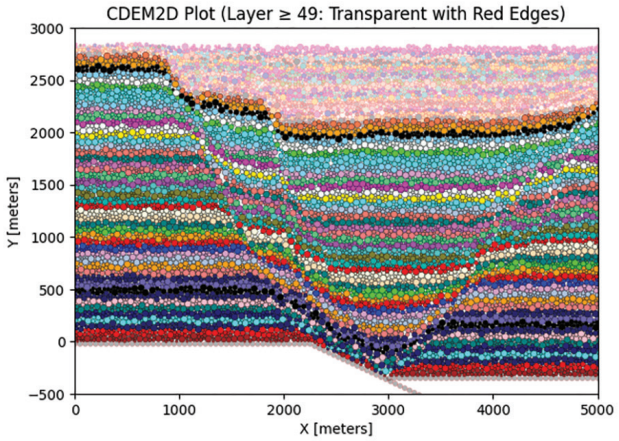

Figure 1 CDEM simulation example illustrating a progressive 30° fault plane normal-fault development and layer offset of ≈450 meters.

The net elastic force on element *i* is the vector sum of normal and shear contributions from every contacting neighbour j:

$$F_i^{el} = \sum_j \left(\mathrm{F_{n,ij}}\hat{\mathrm{n}}_{ij} + \mathrm{F_{s,ij}}\hat{\mathrm{s}}_{ij}\right), \quad (3)$$

to which a viscous damping force $-nx_i$, where η is the damping constant, and a gravitational body force F_g (increasing lithostatic stress with depth) are added. The total force is therefore:

$$F_i = F_i^{el} - \eta\dot{x}_i + F_g \quad (4)$$

and particle motions are advanced with a velocity-Verlet integrator (Allen and Tildesley, 1987). Numerical stability is ensured by choosing the time-step:

$$\Delta t = 0.25\sqrt{\frac{m_{min}}{k_n}} \quad (5)$$

where m_{min} is the smallest particle mass, while η scales as $\Delta t \times 3.0 \times 10^9$/ Ns/m (Table 1 in Cardozo and Hardy, 2023).

After deformation, we estimate a continuum strain field from displacement gradients of element-centre displacements (i.e., ∇u and its symmetric part), used only as a kinematic descriptor; because the elements are rigid, this is not 'particle' strain and we do not update material properties from it. Instead, compressional velocity (V_p) and density (ρ) are assigned by stratigraphic layer, to provide layer-consistent but laterally variable properties. We then rasterise these element-level properties onto a Cartesian grid with cell size $\Delta x = \Delta y \geq 5$, Ravg (at least five times the mean particle radius). For each grid cell, we compute the arithmetic mean of Vp and ρ over all elements whose centres fall inside the cell (empty cells receive the background layer mean). From the gridded fields we compute impedance ($Z = \rho V_p$) and vertical reflectivity ($R = Z_2 - Z_1$), where Z_1 and Z_2 are the impedances of vertically adjacent cells. The resulting reflectivity series is then convolved (1D vertical incidence) with a zero-phase Ricker wavelet to generate the synthetic seismic section.

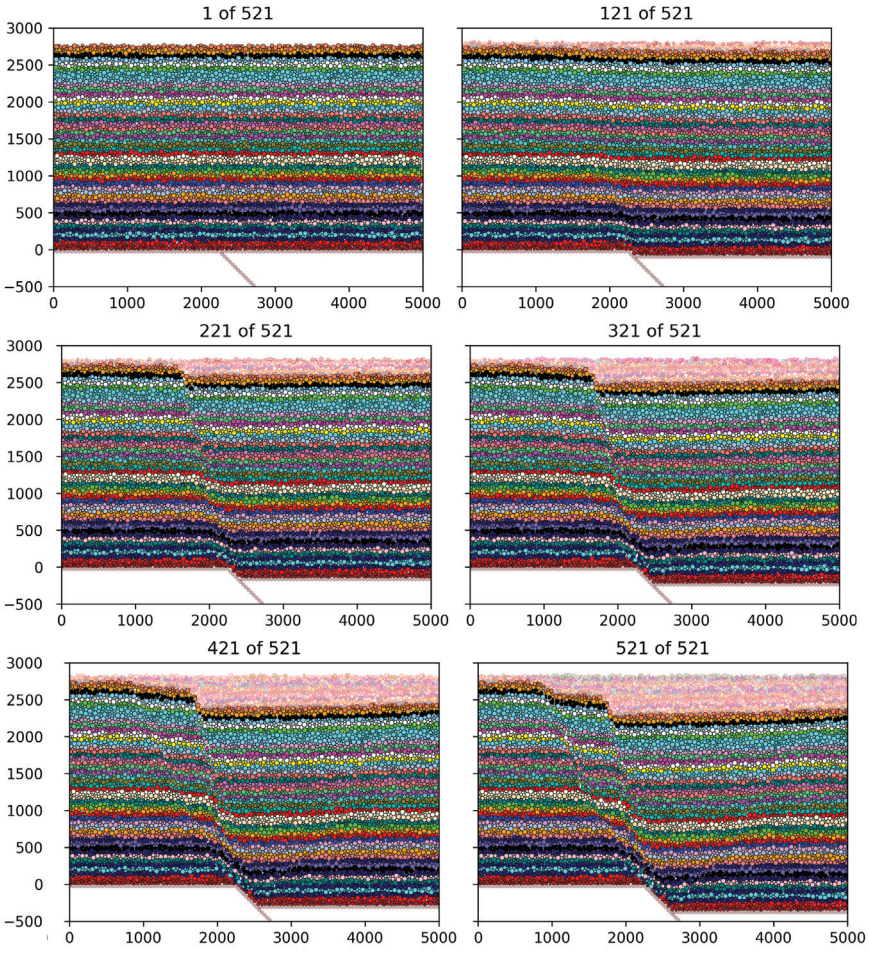

Figure 2 CDEM sequential particle plots at six-time steps illustrating progressive 45° fault plane normal-fault development and layer offset.

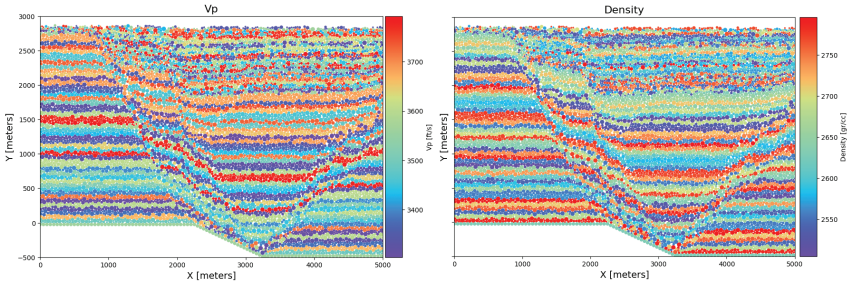

Figure 3 Particle-scale (a) P-wave velocity (Vp) and (b) density distributions after deformation.

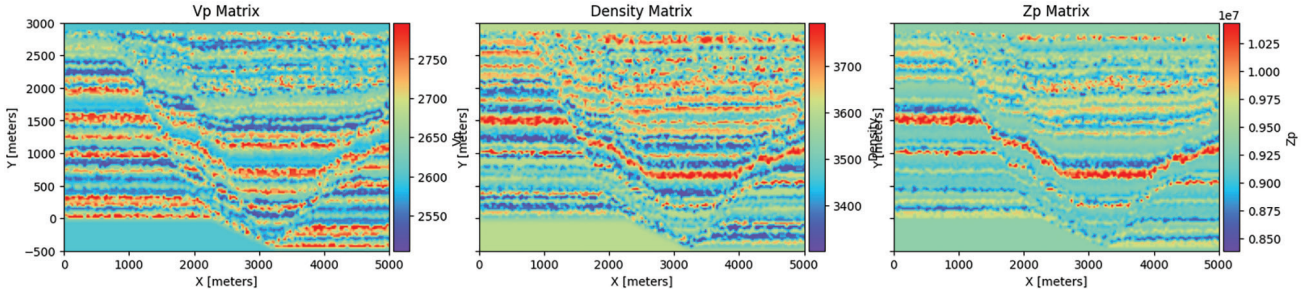

Figure 4 Gridded (a) P-wave, (b) density, and (c) impedance (before filtering), highlighting discretization artefacts.

In this paper, PSDM denotes Pre-Stack Depth Migration, i.e., seismic imaging in depth using the pre-stack wavefield. When we refer to a 'PSDM imaging simulation' (as used in Botter et al., 2014), we mean a ray-based image-processing method. It 'emulates' the PSDM imaging process not by migrating synthetic shots (solving the full wave equation), but by convolving the reflectivity volume with Point-Spread Functions (PSFs) derived from ray tracing. This simulates the specific spatial resolution, diffraction, and illumination effects inherent to a PSDM image of a given survey geometry at low computational cost. By contrast, the 1D convolution used elsewhere in this study captures tuning but not the lateral scattering or survey-dependent illumination effects handled by PSDM.

$$s(t) = (r * w)(t) = \int_{-\infty}^{\infty} r(\tau), w(t-\tau), d\tau\,. \qquad (6)$$

This end-to-end workflow — DEM mechanics, layer-based assignment of rock-physics properties, impedance mapping, reflection modelling, and wavelet convolution — provides a physically grounded route from fault growth to seismic response, capturing amplitude variations.

Results

The starting model is 5 km wide by 2.77 km high, with 48 layers and 10,891 elements (Figure 1). In this example, a 30° normal fault is imposed through boundary displacements, and the model evolves over 521-time increments. In final configuration at step 521, particle-scale is highlighted along the execution of the simulation by an (*x, y*) centre coordinate, its radius, and a group identifier. Irregular fault traces and rotated blocks within a narrow damage zone, absent from kinematic models, are clearly visible.

Figure 2 shows the evolution of deformation at six equally spaced increments (1-521 in steps of 100), for a 45° fault plane normal-fault development. Notice how the layering progressively segments and rotates, with distributed splays and a narrow damage zone forming by time increment 221 and intensifying thereafter. The velocity and density fields inherit this strain localisation; rasterised impedance then transforms it into spatially variable reflectivity. To visualise the model in cross-section, we plot circles whose colours denote stratigraphic 'groups' used for property assignment; elements with the same colour share the same and ρ ranges. Opaque circles represent the original (pre-deposition) elements, whereas semi-transparent circles indicate 'deposited' elements (sediment infill) inserted during the run to fill accommodation generated by hanging- wall subsidence; these deposited elements inherit the property ranges of the layer they infill. Across the six snapshots, deformation progressively localises onto the master fault, accompanied by widening of the damage zone with subsidiary splays and block rotations.

Figure 3 shows the circular particle elements, illustrating that the distributions of the V_p and ρ attributes are equivalent to the results in Figure 1. These scatter plots emphasise the layered impedance stratification and its lateral interference within the fault zone. Rasterisation yields the raw property grids of Figure 4, where abrupt colour changes reflect the discrete sampling of circular elements. We map particle-level ρ and V_p onto a 10 m × 10 m Cartesian grid by evaluating, for each grid cell, the position of its centre (x_c, y_c) relative to every element. If the cell centre falls inside an element's radius, that element's V_p and ρ are accumulated for the cell; after looping over all elements, the sums are divided by the number of contributing elements, so each cell stores the arithmetic mean. Cells with no contributors are set to the background average.

To mitigate the pixel-scale aliasing and small 'holes' introduced by discrete sampling while preserving offsets and sharp boundaries, we apply a light Gaussian filter followed by a small-kernel median filter. This two-step smoothing suppresses high-frequency noise and fills isolated empty values, promoting layer-parallel coherence within units while preserving sharp contrasts and discontinuities at faults and layer terminations. We next compute reflection coefficients by iterating through adjacent cells vertically. Finally, we convolve the reflection coefficients with a Ricker wavelet (peak

frequency of 60 Hz) to simulate a band-limited seismic source and produce synthetic seismic amplitudes.

Figure 5a shows the final bandlimited seismic section, which exhibits the expected oscillatory wavelet character. Strong reflectors near faulted zones or abrupt lithological contrasts cause high amplitudes, while gradual V_p / ρ transitions produce weaker reflections. Figure 5b overlays the DEM elements from Figure 1 on the seismic section of Figure 5a, confirming the tight correspondence between mechanical structure and seismic response.

Frequency sensitivity is illustrated in Figure 6, which shows sections generated with 20, 40, and 60 Hz wavelets across the same time steps as in Figure 1. These frequency-sensitivity results allow us to conclude that, as expected, 20 Hz highlights only gross offsets and broad dimming; 40 Hz begins to resolve major splays and reflector bending; and 60 Hz images minor reflectors inside the damage zone while remaining band-limited. Coherent edge responses that resemble diffraction tails emanate from abrupt terminations at higher frequency, and amplitude dimming beneath the fault core ('amplitude shadows') is visible where strain-related property changes reduce impedance contrast.

Discussion

This synthetic approach goes beyond geometric/kinematic forward modelling commonly used in didactic or quick-look studies—e.g., uniformly tilting horizons or inserting a single planar fault, or applying parameterised folding/faulting to random reflectivity volumes for AI datasets (Vizeu et al., 2022; Wu et al., 2019). Field and outcrop observations show that major faults typically host subsidiary splays, drag, rotated blocks, and heterogeneous damage zones (Kim et al., 2004; Peacock et al., 2017). In our case, the DEM representation reproduces much of this complexity mechanistically, and the resulting seismic response reflects it. However, that expression is inherently limited by resolution constraints set by the finite element size and by the rasterisation grid (10 m cells in our examples), so sub-particle and sub-cell features are not resolved. The steeply dipping master fault is therefore accompanied by irregular offsets and reflector terminations that would not arise in a purely planar model, underscoring the value of physics-based geometries.

Our mechanical-to-seismic workflow shares the conceptual framework of Botter et al. (2014), who coupled DEM, finite-strain rock-physics updates. However, unlike their use of a ray-based PSDM imaging simulation, we employ a simplified 1D convolutional model to study the visibility of fault-zone structure. We similarly link mechanical realism to seismic modelling, but we emphasise computational efficiency and ensemble generation: we deliberately use 1D convolution to accelerate large parameter sweeps while preserving first-order amplitude-frequency behaviour. This makes it tractable to produce many geologically consistent examples for interpretation studies and method development, including machine learning training and benchmarking. In terms of realism, our 1D synthetics reproduce tuning, reflector terminations, and diffraction-like edge responses driven by vertical sampling across lateral terminations, but they do not capture full 3D scattering and survey-dependent illumination that PSDM provides (Lecomte et al., 2015; Botter et al., 2016). Future work will therefore couple

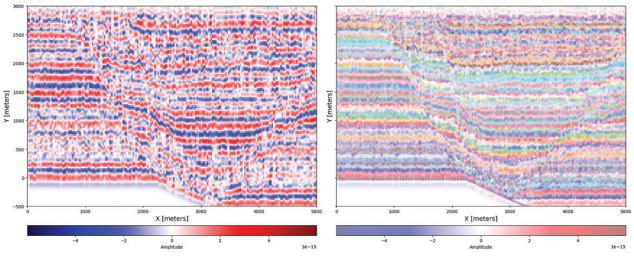

Figure 5 (a) Band-limited synthetic section after 60 Hz zero-phase Ricker convolution. (b) Same section with the final DEM element positions overlain to show the tight correspondence between mechanical and seismic domains.

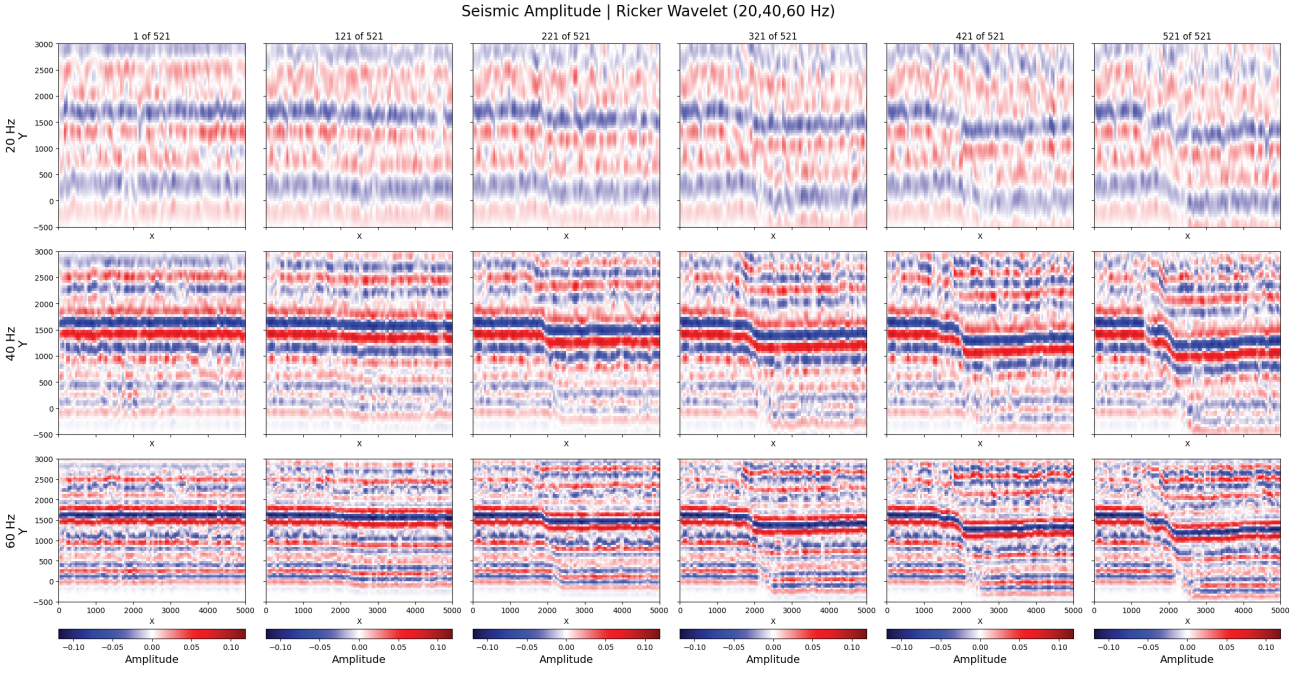

Figure 6 Frequency sensitivity across the deformation sequence. Rows are 20, 40, and 60 Hz; at different time steps.

the same mechanical models to PSDM to quantify the additional effects of lateral wave propagation and acquisition geometry.

Synthetic data derived from mechanically consistent models provide richer and more geologically faithful examples for both training and rigorous evaluation of fault-segmentation networks. By 'stress-testing' we mean benchmarking networks on controlled, labelled DEM- based scenarios that deliberately include difficult case – distributed damage zones, rotated blocks, variable impedance contrasts, tuning and amplitude dimming beneath the fault core, and abrupt reflector terminations – while varying peak frequency (20, 40, 60 Hz), signal-to-noise ratio (SNR), and grid resolution to quantify robustness (precision, recall, IoU) and failure modes. Because the DEM outputs encode distributed deformation and block rotation, and because and vary by layer within realistic ranges, the resulting seismic sections exhibit amplitude shadows, edge responses, and reflector terminations that resemble field data. By contrast, widely used synthetic training sets such as FaultSeg3D are generated by parameterised folding and faulting applied to random reflectivity volumes and do not enforce geomechanical consistency (Wu et al., 2019). Models trained and evaluated on DEM-based synthetics are therefore less likely to overfit to over-simplified geometries and more likely to generalise to field cases, offering a practical route to more robust and geologically reliable fault-segmentation AI models.

Conclusions

By assigning lithology-appropriate properties to DEM elements, updating those properties with finite strain, rasterising to impedance, and applying band-limited 1D convolution, we obtain synthetic sections that reproduce second-order consequences of realistic fault growth. Even with 1D convolution, the sections exhibit strong reflector terminations and coherent edge responses arising from vertical sampling across lateral discontinuities. Although, they are not full diffractions as in PSDM. These characteristics are useful for interpretation and for building geologically grounded datasets for AI training. Future work will couple the same mechanical models to a ray-based PSDM imaging simulation to explicitly incorporate lateral resolution and illumination.

References

Alcalde, J., Bond, C., Johnson, G., Butler, R., Cooper, M. and Ellis. J. [2017]. The importance of structural model availability on seismic interpretation. *Journal of Structural Geology*, **97**, 161-171. https://doi.org/10.1016/j.jsg.2017.03.003.

Allen, M.P. and Tildesley, D.J. [1987]. Computer Simulation of Liquids. Oxford University Press.

Botter, C., Cardozo, N., Hardy, S., Lecomte, I. and Escalona, A. [2014]. From mechanical modelling to seismic imaging of faults: A synthetic workflow to study the impact of faults on seismic. *Marine and Petroleum Geology*, **57**, 187-207, doi: 10.1016/j.marpetgeo.2014.05.013.

Botter, C., Cardozo, N., Hardy, S., Lecomte, I., Paton, G. and Escalona, A. [2016]. Seismic characterisation of fault damage in 3D using mechanical and seismic modeling. *Marine and Petroleum Geology*, **77**, 973-990.

Boyet, A., De Simone, S. and Vilarrasa, V. [2023]. Physics-Based Modelling to Understand and to Propose Forecasting Methods of Induced Seismicity. *Seismological Research Letters*, **94**(6), 2666-2678.

Butler, R. [2023]. Training the creation, visualization and interpretation of fault maps for the subsurface using tectonic geomorphology. *Geological Society, London, Special Publications*, **541**, 181205. https://doi.org/10.1144/SP541-2022-353.

Cardozo, N. and Hardy, S. [2023]. cdem: A macOS program for discrete element modeling of tectonic structures. *Geosphere*, **19**, 1259–1279.

Chopra, S. and Marfurt, K.J. [2007]. Volumetric curvature attributes for fault/fracture characterization. *First Break*, **25**(7), 35-46.

Couples, G., Ma, J., Lewis, H., Olden, P., Quijano, J., Fasae, T. and Maguire, R. [2007]. Geomechanics of faults: impacts on seismic imaging. *First Break*, **25**(10), 83-90. https://doi.org/10.3997/1365-2397.25.10.27671

Cundall, P.A. and Strack, O.D.L. [1979]. A discrete numerical model for granular assemblies. *Geotechnique*, **29**, 47-65.

Diao, F., Weng, H., Ampuero, J.P., Shao, Z., Wang, R., Long, F. and Xiong, X. [2024]. Physics-based assessment of earthquake potential on the Anninghe-Zemuhe fault system in southwestern China. *Nature Communications*, **15**(1), 6908.

Dutzer, J.F., Basford, H. and Purves, S. [2010]. Investigating fault-sealing potential through fault relative seismic volume analysis. *Geological Society, London, Petroleum Geology Conference Series*, **7**, 509-515. https://doi.org/10.1144/0070509

Egholm, D.L., Sandiford, M., Clausen, O.R. and Nielsen, S.B. [2008]. A new strategy for discrete-element numerical models: 2. Sandbox applications. *Journal of Geophysical Research*, **112**, B05204.

Ercoli, M., Carboni, F., Akimbekova, A., Carbonell, R.B. and Barchi, M.R. [2023]. Evidencing subtle faults in deep seismic reflection profiles: Data pre-conditioning and seismic attribute analysis of the legacy CROP-04 profile. *Frontiers in Earth Science*, **11**, 1119554. https://doi.org/10.3389/feart.2023.1119554.

Faulkner, D.R., Jackson, C.A.L., Lunn, R.J., Schlische, R.W., Shipton, Z.K., Wibberley, C.A.J. and Withjack, M.O. [2010]. A review of recent developments concerning the structure, mechanics and fluid flow properties of fault zones. *J. Struct. Geol.*, **32**, 1557-1575.

Ferrill, D., McGinnis, R., Morris, A., Smart, K., Sickman, Z., Bentz, M., Lehrmann, D. and Evans, M. [2014]. Control of mechanical stratigraphy on bed-restricted jointing and normal faulting: Eagle Ford Formation, south-central Texas. *AAPG Bulletin*, **98**, 2477-2506, doi: 10.1306/08191414053.

Freeman, B., Boult, P.J., Yielding, G. and Menpes, S. [2010]. Using empirical geological rules to reduce structural uncertainty in seismic interpretation of faults. *Journal of Structural Geology*, **32**(11), 1668-1676.

Gong, L, Bo, L., Xiaofei, F., Hadi, J., Shuai, G., Wenting, Y., Hongqi, Y., Rongzhi, F. and Zijie, W. [2019]. Quantitative prediction of sub-seismic faults and their impact on waterflood performance: Bozhong 34 oilfield case study. *Journal of Petroleum Science and Engineering*, **172**, 60-69, https://10.1016/j.petrol.2018.09.049.

Gudmundsson, A., Simmenes, T., Larsen, B. and Philipp, S. [2010]. Effects of internal structure and local stresses on fracture propagation, deflection, and arrest in fault zones. *Journal Structural Geology*, **32**, 1643–1655, doi: 10.1016/j.jsg.2009.08.013.

Gunderson, K.L., Zhang, Z., Payne, B., Cheng, S., Jiang, Z. and Wang, A. [2022]. Machine learning applications to seismic structural interpretation: Philosophy, progress, pitfalls, and potential Available to Purchase. *AAPG Bulletin*, **106**(11), 2187–2202. https://doi.org/10.1306/12162121016.

Hardy, S. [2008]. Structural evolution of calderas: Insights from two-dimensional discrete element simulations. *Geology*, **36**, 927-930. https://doi.org/10.1130/G25133A.1.

Hardy, S. [2016]. Does shallow dike intrusion and widening remain a possible mechanism for graben formation on Mars? *Geology*, **44**, 107-110, https://doi.org/10.1130/G37285.1.

Hardy, S. [2018]. Coupling a frictional-cohesive cover and a viscous substrate in a discrete-element model. *Marine and Petroleum Geology*, **97**, 32-44.

Hardy, S. [2019a]. Novel discrete element modeling of Gilbert-type delta formation in an active tectonic setting First results. *Basin Research*, **31**(1), 77-91, https://doi.org/10.1111/bre.12309.

Hardy, S. [2019b]. Discrete element modeling of extensional, growth, fault-propagation folds. *Basin Research*, **31**(3), 584-599. https://doi.org/10.1111/bre.12335.

Hardy, S. and Finch, E. [2007]. Mechanical stratigraphy and the transition from trishear to kink-band fault-propagation fold forms above blind basement thrust faults: A discrete-element study. *Marine and Petroleum Geology*, **24**, 75-90. https://doi.org/10. 1016/j.marpetgeo.2006.0.

Hardy, S., McClay, K. and Muñoz, J.A. [2009]. Deformation and fault activity in space and time in high-resolution numerical models of doubly vergent thrust wedges. *Marine and Petroleum Geology*, **26**(2), 232-248. https://doi.org/10.1016/j.marpetgeo.2007.12.003.

Iacopini, D. and Butler, R.W.H. [2011]. Imaging deformation in submarine thrust belts using seismic attributes. *Earth and Planetary Science Letters*, **302**, 414-422. https://doi. org/10.1016/j.epsl.

Kanasewich E. and Phadke, S. [1988]. Imaging discontinuities on seismic sections. *Geophysics*, **53**(3), 290-416. https://doi.org/10.1190/1.1442467

Khosro Anjom, F., Vaccarino, F. and Socco, L.V. [2024]. Machine learning for seismic exploration: Where are we and how far are we from the holy grail? *Geophysics*, **89**(1), WA157-WA178.

Kim, Y., Peacock, D. and Sanderson, D. [2004], Fault damage zones. *Journal Structural Geology*, **26**, 503–517. https://10.1016/j.jsg.2003.08.002.

Lecomte, I., Lavadera, P.L., Anell, I., Buckley, S.J., Schmid, D.W. and Heeremans, M. [2015]. Ray-based seismic modeling of geologic models: Understanding and analysing seismic images efficiently. *Interpretation*, **3**(4), SAC71-SAC89.

Li, W., Yue, D., Colombera, L., Duan, D., Long, T., Wu, S. and Liu, Y. [2023]. A novel method for seismic-attribute optimization driven by forward modeling and machine learning in prediction of fluvial reservoirs. *Geoenergy Science and Engineering*, **227**, 211952. https://doi.org/10.1016/j.geoen.2023.211952.

Liu, X. and Konietzky, H. [2018]. DEM investigation on strike-slip fault mechanics. *Tectonophysics*, **722**, 283–298.

Long, J.J. and Imber, J. [2010]. Geometrically coherent continuous deformation in the volume surrounding a seismically imaged normal fault-array. *Journal of Structural Geology*, **32**(2), 222-234. https://doi.org/10.1016/j.jsg.2009.11.009.

Ma, L., Han, L. and Feng, Q. [2024]. Deep learning for high-resolution seismic imaging. *Scientific Report*, **14**. https://10.1038/s41598-024-61251-8.

Mirkamali, M.S., Javaherian, A., Hassani, H., Saberi, M.R. and Sarallah-Zabihi, S. [2023]. Seismic forward modeling for investigating and interpreting thin beds in a carbonate reservoir in SW Iran. *Exploration Geophysics*, **54**(6), 601-624.

Mora, P. and Place, D. [1993]. A lattice solid model for the non-linear dynamics of earthquakes. *Int. J. Mod. Phys. C*, **4**(6), 1059-1074.

Mora, P. and Place, D. [1994]. Simulation of the frictional stick-slip instability. *Pure and Applied Geophysics*, **143**, 61–87.

Morgan, J.K. and Boettcher, M.S. [1999]. Numerical simulations of granular-shear experiments. *Tectonophysics*, **324**, 299-322.

North, F.K. [1985]. *Petroleum Geology*. Allen & Unwin, Boston.

Oakley, D., Cardozo, N., Vazquez, A.A. and Røe, P. [2023]. Structural geologic modeling and restoration using ensemble Kalman inversion. *Journal of Structural Geology*, **171**, 104868. https://doi.org/10.1016/j.jsg.2023.104868.

Paxton, A., Zhang, L., Kholiq, A., Davey, L., Bisley, R., Fell, D., Leon, L. and Shadlow, J. [2022]. November. Reducing seismic quantitative interpretation uncertainty in complex geological environments: A case study from offshore Australia. In SEG International Exposition and Annual Meeting (D011S116R003).

Peacock, D., Nixon, C., Rotevatn, A., Sanderson, D. and Zuluaga, L. [2017]. Interacting faults. *Journal of Structural Geology*, **97**, 1-22, doi: 10.1016/j.jsg.2017.02.008.

Perez Altamar, R., Wiebe, M. and Pablos Corredor, A. [2024]. Integration of deep-learning fault segmentation, horizontal transverse isotropy analysis, and ambient microseismic methods to enhance fracture prediction in the Crisol Anticline, Colombia. *Interpretation*, **12**, SD1-SD16. https://doi.org/10.1190/INT-2023-0046.1.

Place, D., Lombard, F., Mora, P. and Abe, S. [2002]. Simulation of the micro-physics of rocks using LSMEarth. *Pure and Applied Geophysics*, **159**, 1911–1932.

Planke, S., Rasmussen, T., Rey, S.S. and Myklebust, R. [2005]. Seismic characteristics and distribution of volcanic intrusions and hydrothermal vent complexes in the Vøring and Møre basins. In: Dor´e, A.G. and Vining, B. (Eds.) Petroleum Geology: North-West Europe and Global Perspectives. *Proceedings of the 6th Petroleum Geology Conference*, Geological Society, London, 833-844.

Reicherter, K., Ritter, J.R., Baize, S., Steinritz, V., Pena-Castellnou, S. and Hürtgen, J. [2023]. Clustered activity of Intraplate Faults: The silent and slow active faults of southern Germany. *Abstracts of the Annual AlpArray and 4D-MB Scientific Meeting*, Bad Hofgastein.

Romberg, R. [2002]. Challenges in high-resolution seismic imaging of complex structures. *First Break*, **20**, 567-574.

Slejko, D., Carulli, G.B., Garcia, J. and Santulin, M. [2011]. The contribution of "silent" faults to the seismic hazard of the northern Adriatic Sea. *Journal of Geodynamics*, **5**, 2-3, 166-178. https://doi.org/10.1016/j.jog.2010.04.009.

Townsend, C., Firth, I.R., Westerman, R., Kirkevollen, L., Hårde, M. and Andersen, T. [1998]. Small seismic-scale fault identification and mapping. *Geological Society, London, Special Publications*, **147**, 1-25. https://doi.org/10.1144/GSL.SP.1998.147.01.0.

Vizeu, F., Zambrini, J., Tertois, A.L., da Graça e Costa, B.D.A., Fernandes, A.Q. and Canning, A. [2022]. Synthetic seismic data generation for automated AI-based procedures with an example application to high-resolution interpretation. *The Leading Edge*, **41**(6), 392-399.

Wu, X., Liang, L., Shi, Y. and Fomel, S. [2019]. FaultSeg3D: Using synthetic data sets to train an end to end convolutional neural network for 3D seismic fault segmentation. *Geophysics*, **84**(3), IM35–IM45. https://doi.org/10.1190/geo20180646.1.

Zeng, L. and H. Liu. [2010]. Influence of fractures on the development of low-permeability sandstone reservoirs: A case study from the Taizhao district, Daqing Oilfield, China. *Journal of Petroleum Science and Engineering*, **72**, 120-127, doi: 10.1016/j.petrol.2010.03.009.